This is an open access article published under an ACS AuthorChoice License, which permits copying and redistribution of the article or any adaptations for non-commercial purposes.

JACS
JOURNAL OF THE AMERICAN CHEMICAL SOCIETY

Article

pubs.acs.org/JACS

Cobalt–Iron (Oxy)hydroxide Oxygen Evolution Electrocatalysts: The Role of Structure and Composition on Activity, Stability, and Mechanism

Michaela S. Burke,[†] Matthew G. Kast,[†,‡] Lena Trotochaud,[†] Adam M. Smith,[†] and Shannon W. Boettcher*[,†,‡]

[†]Department of Chemistry and Biochemistry and [‡]Center for Sustainable Materials Chemistry, University of Oregon Eugene, Oregon 97403, United States

Supporting Information

ABSTRACT: Cobalt oxides and (oxy)hydroxides have been widely studied as electrocatalysts for the oxygen evolution reaction (OER). For related Ni-based materials, the addition of Fe dramatically enhances OER activity. The role of Fe in Co-based materials is not well-documented. We show that the intrinsic OER activity of $Co_{1-x}Fe_x(OOH)$ is ~100-fold higher for $x \approx 0.6–0.7$ than for $x = 0$ on a per-metal turnover frequency basis. Fe-free CoOOH absorbs Fe from electrolyte impurities if the electrolyte is not rigorously purified. Fe incorporation and increased activity correlate with an anodic shift in the nominally $Co^{2+/3+}$ redox wave, indicating strong electronic interactions between the two elements and likely substitutional doping of Fe for Co. *In situ* electrical measurements show that $Co_{1-x}Fe_x(OOH)$ is conductive under OER conditions (~0.7–4 mS cm^{-1} at ~300 mV overpotential), but that FeOOH is an insulator with measurable conductivity (2.2×10^{-2} mS cm^{-1}) only at high overpotentials >400 mV. The apparent OER activity of FeOOH is thus limited by low conductivity. Microbalance measurements show that films with $x \geq 0.54$ (i.e., Fe-rich) dissolve in 1 M KOH electrolyte under OER conditions. For $x < 0.54$, the films appear chemically stable, but the OER activity decreases by 16–62% over 2 h, likely due to conversion into denser, oxide-like phases. We thus hypothesize that Fe is the most-active site in the catalyst, while CoOOH primarily provides a conductive, high-surface area, chemically stabilizing host. These results are important as Fe-containing Co- and Ni-(oxy)hydroxides are the fastest OER catalysts known.

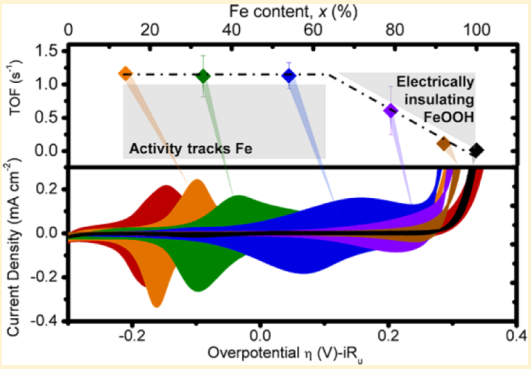

1. INTRODUCTION

Water splitting by direct or photodriven electrolysis ($2H_2O \rightarrow O_2 + 2H_2$) provides a potential path for the production of clean, renewable H_2 fuel to power human civilization.[1−5] The efficiency of water electrolysis is limited, in part, by the high kinetic overpotential associated with driving the oxygen evolution reaction (OER).[3,6−12] In addition to facilitating fast kinetics (i.e., low overpotential), ideal OER catalysts are composed of nontoxic earth-abundant elements, economical to manufacture, chemically and mechanically stable, and sufficiently electrically conductive to facilitate integration with water-splitting (photo)anodes.[13−17]

Although water electrolysis can, in principle, be performed in conductive electrolytes of any pH, alkaline conditions are perhaps best suited to meet the above requirements. In neutral electrolytes, the slow transport of buffer ions and the formation of a pH gradient (particularly when membranes to separate H_2 from O_2 are used) increase the cell resistance and lower efficiency.[2,18] Membranes with high H^+ mobility (e.g., Nafion)[19] are used for commercial water electrolyzers in acidic conditions.[20,21] Unfortunately, the scarce and expensive IrO_2-based catalysts used are the only known acid-insoluble OER catalysts with reasonable activity.[17,22]

In contrast, many inexpensive, earth-abundant, first-row transition metals are OER active and largely insoluble in alkaline electrolytes.[3,13,14,16,17,23,24] Independent of synthetic method, transition metals and their oxides often form (oxy)hydroxides at their surfaces in alkaline solutions during OER. These surface structures are different than those of the bulk crystalline oxide phases.[3,25−27] Such structural transformations under catalytically relevant conditions make mechanistic studies at these surfaces challenging.

Co-based OER catalysts, e.g. Co–P_i (electrodeposited CoO_x films in a phosphate electrolyte),[28] have been of recent interest due to reasonable activity and catalyst "self-repair" in neutral electrolyte.[29] Substantial work has aimed to understand the relation between structure, mechanism, and activity.[30−37] Co–P_i and related catalysts are composed of small fragments/layers of CoOOH during OER, independent of initial deposition

Received: January 9, 2015
Published: February 20, 2015

 © 2015 American Chemical Society

DOI: 10.1021/jacs.5b00281
J. Am. Chem. Soc. 2015, 137, 3638−3648

conditions or the electrolyte used.[27,38−41] Klingan et al. showed that the "bulk" material is active for catalysis because it consists of a mixture of electrolyte-accessible CoOOH nanosheets, counterions, and electrolyte.[39] Risch et al. complemented this analysis using X-ray absorption spectroscopy to follow the Co oxidation state and local structure during the OER.[42]

Mixed-metal systems containing both Co and Fe have also been studied in basic media. There are conflicting reports as to whether the addition of Fe into CoO_x increases OER activity, due to the difficultly in quantifying the number of active sites, the surface/local structures under which OER occurs, and the catalyst stability as a function of Fe content. Several studies show that the addition of Fe to polycrystalline Co_3O_4 decreased the Tafel slope.[43−46] Kishi et al. concluded that the addition of Fe in $Fe_xCo_{3-x}O_4$ ($0 \leq x \leq 2$) decreased OER actvitiy.[47] Smith et al. report little difference in Tafel slope between photochemically deposited porous/amorphous CoO_x, FeO_x, and $FeCoO_x$[48] (likely a mix of oxides and (oxy)hydroxides). In a later study, they showed that the $FeCoO_x$ and CoO_x films have the same overpotential (0.27 ± 0.02 V) at 1 mA cm^{-2} anodic current density.[49] McCrory et al. benchmarked different OER catalysts and found that the overpotential at 10 mA cm^{-2} (geometric surface area) for CoO_x and $CoFeO_x$ was statistically indistinguishable (0.39 ± 0.04 and 0.37 ± 0.02 V, respectively).[17] At lower overpotentials (350 mV), however, McCrory et al. note that $CoFeO_x$ has ∼7-fold higher current density than CoO_x. Suntivich et al. reported high activity from a $Ba_{0.5}Sr_{0.5}Co_{0.8}Fe_{0.2}O_x$ perovskite catalyst optimized based on molecular orbital principles.[50] Further work from the same group showed that Ba^{2+} and Sr^{2+} leached at the surface, leaving behind amorphous Fe−Co phases, likely (oxy)hydroxides, which were responsible for the measured OER activity.[51]

Fe is known to have a dramatic effect on the OER activity of Ni-based materials by substituting for Ni in NiOOH.[52,53] This is intriguing as alone, NiOOH is a very poor OER catalyst,[53] while FeO_x is also traditionally considered to have low OER activity.[54] Evidence from our group[53] and others[52,55−57] shows that Fe affects the local electronic structure of the NiOOH, suggesting the possibility that Fe (or Ni substantially modified by the presence of Fe) is the active site. Unaccounted for Fe impurities have also complicated attempts to elucidate the OER mechanism on Ni-based materials. An improved understanding of the role that Fe (and other) additives/impurities play in OER catalysis is thus important for implementing new approaches to enhance catalytic activity. Given the volume of work on CoO_x electrocatalysis and the record-high OER activity of the related Ni(Fe)OOH materials, it is particularly important to clarify the role of Fe in OER on Co(Fe)OOH.

Here, we probe the role of structure and composition in $Co_{1-x}Fe_x(OOH)$ films electrodeposited on quartz-crystal microbalance (QCM) electrodes in alkaline media. We follow the activity, voltammetry, stability, conductivity, morphology, and chemical changes that occur during OER catalysis. We use total film mass to calculate approximations of intrinsic activity for the different possible active cations. We discover that Fe incorporation increases the intrinsic activity of CoOOH by ∼100-fold, with peak activity for 40−60% Fe. Based on *in situ* mass measurements, we find that Fe also affects chemical and structural stability. $Co_{1-x}Fe_x(OOH)$ films with $x > 0.54$ slowly dissolve under anodic polarization, while those with lower x appear insoluble. *In situ* measurements of electrocatalyst film conductivity show that while $Co_{1-x}Fe_x(OOH)$ ($x > 1$) is conductive under OER conditions, FeOOH only has measurable conductivity at overpotentials >400 mV. The intrinsic activity of FeOOH at low overpotentials is thus masked by high electrical resistance. This may indicate that the CoOOH (and similarly NiOOH) serves primarily as electrically conductive and chemically stable host that enhances the activity of Fe-based active sites in the most-active mixed-cation phases. These results thus shed light onto the role of Fe in high-activity $Co_{1-x}Fe_x(OOH)$ OER catalysts and provide further basis for the rational development of new catalysts with improved activity.

2. EXPERIMENTAL SECTION

2.1. Solution Preparation. A stock solution of 0.1 M $Co(NO_3)_2 \cdot 6H_2O$ (Strem Chemicals, 99.999% trace metal basis) was prepared in 18.2 MΩ·cm water. Individual solutions of mixed $Co(NO_3)_2$ and $FeCl_2$ (total 0.1 M metal ion concentration) for $Co_{1-x}Fe_x(OH)_2$ films of $x > 0$ and 0.1 M $FeCl_2$ (Sigma-Aldrich, > 98%) and 0.05 M $NaNO_3$ (Mallinckrodt Chemicals, > 98%) for $x = 1$ were freshly prepared in 18.2 MΩ·cm water for each deposition session (<10 film depositions per session). The $FeCl_2$ solutions are air sensitive and form FeOOH precipitates in the presence of oxygen.[53] All solutions containing $FeCl_2$ were covered in Parafilm and purged with N_2 for ∼20 min prior to $FeCl_2$ addition and between depositions. $NaNO_3$ was added to $FeCl_2$ solutions to facilitate the cathodic deposition via reduction of NO_3^-.[53,58]

2.2. Film Electrodeposition. $Co_{1-x}Fe_x(OH)_2$ was cathodically deposited onto Au/Ti-coated 5 MHz QCM crystals (Stanford Research Systems QCM200) using a two-electrode cell with a carbon-cloth counter electrode (Fuel Cell Earth, untreated).[53] Deposition was accomplished by applying between −0.1 and −4.0 mA cm^{-2} (cathodic) until the desired mass was registered on the QCM.[52,58−60] Deposition rates vary for optimal substrate coverage and are indicated in Table S1. The film masses (∼10 $\mu g\ cm^{-2}$) were calculated based on the Sauerbrey equation ($\Delta f = -C_f \times \Delta m$, where Δf is the experimental frequency change, C_f is the sensitivity factor, 64.5 Hz $cm^2\ \mu g^{-1}$, of the 5 MHz AT-cut quartz crystal in solution, and Δm is the change in mass per area, see Figure S1 and corresponding example mass calculations).[16,61] Mass is lost during the first cycle, which we attribute to residual ion (e.g., nitrate, chloride) loss to the solution (Figure S2). The film mass was thus determined from the difference between the measured QCM resonance frequency in 18 MΩ·cm water prior to deposition and that after the first voltammetry cycle (Figure S1 and supporting calculations). Prior to deposition, all QCM crystals were cleaned in 1 M H_2SO_4 (Sigma-Aldrich) via potential cycling (2 cycles, 2.5 to −2.5 V at 200 mV s^{-1}). The Au/Ti QCM crystals were then cycled in 1 M KOH to check for the appropriate Au redox features and confirm the absence of any redox features or OER current associated with residual impurities or Co from previous measurements (see Figure S3), rinsed in 18.2 MΩ·cm water, and transferred to the deposition solution. It was also found that Co (and Fe) from the deposition solution readily adsorbed to the Teflon QCM holder and would contaminate the electrolyte when transferred to the electrochemical testing cell, resulting in inconsistent experimental results. To prevent this, the QCM holder was quickly removed after deposition from the acidic deposition solution (which slowly dissolves the film) and submerged into three consecutive 18.2 MΩ·cm water baths to rinse off excess deposition solution. The crystal was then transferred to a second, acid-cleaned Teflon QCM holder for use in the electrochemical testing cell. Films characterized *ex situ* prior to further electrochemical measurements are referred to as "as-deposited" samples (Table S1).

2.3. Electrochemical Characterization. Measurements were made with a potentiostat (BioLogic SP300 or SP200) using a three electrode (voltammetry and steady-state studies) or four electrode (through-film conductivity studies) cell with a coiled Pt-wire counter electrode contained in a plastic fritted compartment and a Hg/HgO reference electrode (CH Instruments) filled with 1 M KOH. For activity measurements the electrolyte was saturated with ultrahigh

DOI: 10.1021/jacs.5b00281
J. Am. Chem. Soc. 2015, 137, 3638−3648

purity O_2 (sparged ~20 min prior to the experiment and continuously bubbled during the data collection). Magnetic stirring was used to eliminate bubble accumulation. Through-film conductivity measurements were made using Au/Ti/quartz interdigitated array (IDA) electrodes (CH instruments, 2 μm electrode width, 2 μm gap, 2 mm length, 65 pairs). The conductivity was extracted from the steady-state current between the two working electrodes with a 10 mV offset during which the potential of both were stepped between 0 and 0.65 V (2−5 min per step). The conductivity of the FeOOH was not sufficient to measure in this way due to low effective conductivity at low overpotentials and the interference from the comparatively large OER current at high overpotentials. Alternatively, we first poised both working electrodes at the same potential until a steady-state OER current was reached. We then stepped the potential of the first electrode by 10 mV, causing a significant change in OER current on that electrode. The change in current on the second electrode was assumed to be only due to electrical transport through the FeOOH from one working electrode to the other, because the potential of the second electrode was not changed. We confirmed this by measuring a number of different positive and negative potential step combinations (see Figure S4 for details). This method allows for measurement of the small conductance current on top of the large OER background current.

All electrochemical measurements were made in polytetrafluoroethylene (PTFE) or Nalgene containers. No glass components were used as they are etched in 1 M KOH and contaminate the electrolyte with Fe and other impurities. All plastic components were cleaned with 1 M H_2SO_4 prior to use. Pt counter electrodes were regularly cleaned by dipping briefly (~5 s) in aqua regia. The Hg/HgO reference electrode was calibrated against a reversible hydrogen electrode (RHE) at pH 14 (0.93 V vs RHE), fabricated by bubbling H_2(g) over a freshly cleaned Pt electrode. When indicated, measurements were corrected for uncompensated series resistance (R_u). R_u was determined by equating R_u to the minimum impedance between 10 kHz and 1 MHz, where the phase angle was closest to zero. R_u was between 2 and 6 Ω for QCM electrodes. Current densities were calculated using the geometric surface area of the QCM crystal (1.38 cm^2). The overpotential (η) was calculated where $\eta = E_{measured} - E_{rev} - iR_u$. $E_{measured}$ is the recorded potential vs Hg/HgO and E_{rev} is the reversible potential (0.30 V vs Hg/HgO) for the OER.[1] All three-electrode steady-state potentiostatic experiments were corrected for iR_u in real time using a manual iR compensation based on the full value of R_u derived from the impedance measurements.

2.4. Purification of KOH Electrolyte. As-received KOH (Sigma TraceSelect or Semiconductor grade), diluted to 1 M, was used for all measurements made on films already containing Fe because these films did not absorb a discernible amount of Fe from solution. Electrochemical measurements performed on Fe-free samples used purified 1 M KOH, unless the film was being tested for Fe accumulation in the as-received electrolyte. The 1 M KOH was purified as follows. $Co(OH)_2$ was precipitated from $Co(NO_3)_2$ (0.5−1 g, 99.999%) with ~0.1 M KOH and washed three times via mechanical agitation, centrifugation, and decanting. The triple-washed $Co(OH)_2$ was then added to the 1 M KOH electrolyte and mechanically agitated for 10 min to absorb Fe impurities (the affinity for Fe by $Co(OH)_2$ is demonstrated below). The resultant brown suspension was centrifuged for 1 h, and the Fe-free electrolyte decanted into a clean PTFE electrochemical test cell for use. This procedure is analogous to the KOH cleaning procedure developed using $Ni(OH)_2$,[53] however, it eliminates the possibility of Ni contamination by using $Co(OH)_2$.

2.5. Materials Characterization. Scanning electron microscope (SEM) images were taken using a Zeiss Ultra 55 SEM operating at 5 keV. Compositional information (Fe/Co ratio) was determined by X-ray photoelectron spectroscopy (XPS) with an ESCALAB 250 (ThermoScientific) using a Mg Kα nonmonochromated flood source (400 W, 75 eV pass energy). An Al Kα monochromated source (150 W, 20 eV pass energy, 500 μm spot size) was used to collect oxidation state information. All samples were charge neutralized using an in-lens electron source and grounded to the stage with a conductive clip to minimize charging. The resulting spectra were analyzed with a Shirley background, calibrated using the substrate Au 4f peaks (84.0 eV), and peak fit using ThermoScientific Avantage 4.75 software. The Mg Kα source was used for determining the Fe/Co ratio because the Al Kα source yields large Co or Fe Auger (LMM Co at 713 eV and Fe at 784 eV)[62] peaks that overshadow smaller Fe 2p or Co 2p peaks, respectively. Grazing incidence X-ray diffraction (GIXRD) patterns were taken on thick films using a Rigaku SmartLab diffractometer (0.4° incident angle, 0.1° step size, and 120 s per step integration time) with parallel beam optics, diffracted-beam monochromator (to remove Fe fluorescence), knife edge, and K-β filter. Thick films for GIXRD of x = 0, 0.54, and 1.0 were deposited for 15, 10, and 20 min, respectively, onto Au/Ti/glass slides at a specified current density (−2, −4, and −1 mA cm^{-2}, respectively). All glass components in premade electrodes were covered with hot glue to eliminate Fe contamination we found from Hysol 1C epoxy that is typically used in our laboratory.

3. RESULTS AND DISCUSSION

3.1. Film Preparation and Structural Characterization. The study of OER electrocatalysts has been hampered by difficulties in accurately identifying the catalytically active phases. When oxides prepared at high-temperature are used as OER catalysts in base, a surface layer that is the active catalyst usually forms that is composed of (oxy)hydroxides, as predicted by equilibrium Pourbaix diagrams[63] and as has been observed directly in several cases.[16,51,64,65] Measurements of chemical structure and composition of this surface layer can be challenging, however, as the underlying bulk crystalline phase often dominates the signal for many analysis techniques.

To address this, we directly electrodeposited hydrated Co−Fe (oxy)hydroxides at room temperature and studied them electrochemically without dehydration or heating. The deposition proceeds via the cathodic reduction of NO_3^- at the electrode surface which increases the pH to drive metal hydroxide precipitation at the electrode surface.[58,66,67] Although the Fe/Co ratio in solution was typically higher than that of the deposited material, films deposited from the same solutions had similar Fe content within 2% (Table S1).

GIXRD patterns of as-deposited $Co_{1-x}Fe_x(OH)_2$ with x = 0, 0.54, and 1.0 are plotted in Figure 1a. No reflections from the Au−Ti substrates are observed in the range shown (reference patterns can be found in Figure S5). The diffraction pattern for the x = 0 sample (as deposited) has a broad peak centered at d = 5.1 Å corresponding roughly to the 001 reflection of β-$Co(OH)_2$. The sharp peak at d = 4.2 Å and the collection of peaks at ~2.7−2.6 Å suggest also the presence of α-$Co(OH)_2$.[60] The broadness of the peak between 7.5−4.4 Å suggests variation in the local d-spacing associated with nonhomogeneous intercalation of water and/or ions in a somewhat disordered α-$Co(OH)_2$ material.[60,68] The pattern for the x = 0.54 sample has two distinct low-angle peaks (d = 7.7 and 4.2 Å) consistent with the (003) and (006) reflections from a Co−Fe fougèrite-analogue phase in which Fe^{3+} substitutes for Co^{2+}. The pattern for the x = 1 sample (Fe-only) has a number of peaks that can be well-indexed to a mix of α, β, and γ FeOOH (Figure S5).

SEM imaging shows that the as-deposited films consist of platelets roughly 100 nm in diameter that tend to be vertically oriented and randomly distributed on the electrode surface (Figure 1b, top row and Figure S6). This morphology is consistent with that typically observed for layered double hydroxides or oxyhydroxides adopting a brucite-like structure with octahedrally coordinated metal cations hexagonally packed in sheets that are separated by water and charge-balancing ions.[58,67−73] The morphology is not substantially altered by

DOI: 10.1021/jacs.5b00281
J. Am. Chem. Soc. 2015, 137, 3638−3648

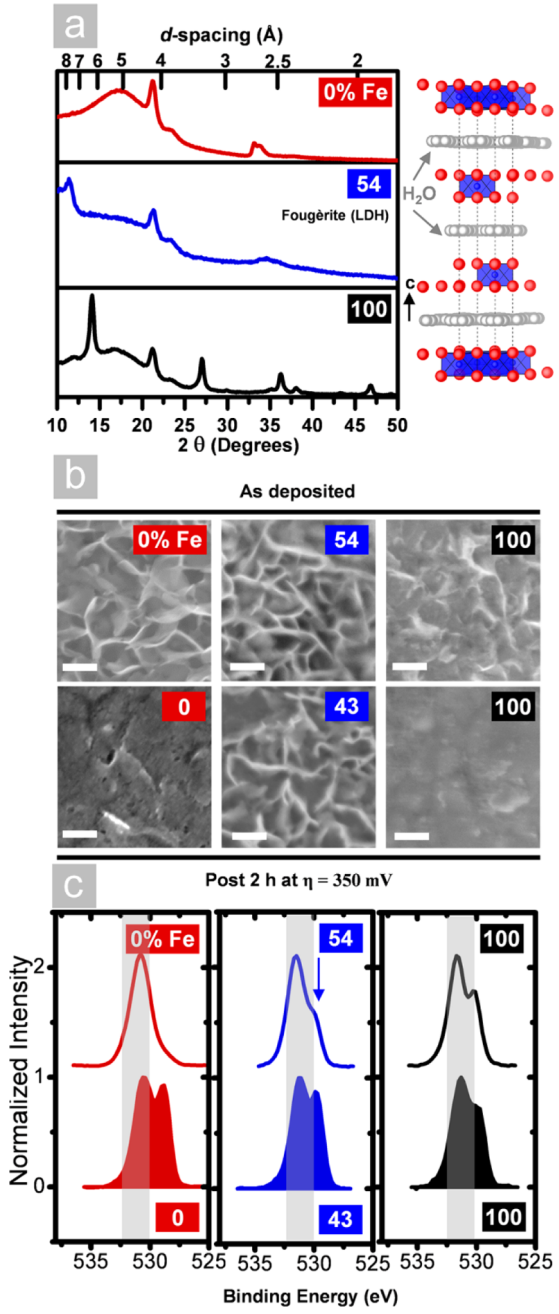

Figure 1. Materials characterization of electrodeposited $Co_{1-x}Fe_x(OH)_2/Co_{1-x}Fe_xOOH$ films. (a) GIXRD of as-deposited films (see Figure S5 for indexed patterns) where x = 0, 0.54, 1 (left), and crystal structure for layered double hydroxide x = 0.54 (fougèrite, ICSD 159700, all Fe analog) along the [100] direction (right). The unit cell is indicated by dotted lines, red = OH; blue = Fe^{3+}/Co^{2+}; gray = water. (b) SEM images of samples as-deposited (top) and after 2 h of anodic polarization at η = 350 mV (bottom). The scale bars are 100 nm (see Figures S6 and S8 for full composition set). (c) O 1s XP spectra of samples as-deposited (top) and after 2 h anodic polarization (bottom). Gray shading indicates the peak for hydroxide phases (see Figure S7 for full composition set).

addition of Fe, suggesting a solid solution. The O 1s XPS spectra of the film as-deposited from pure $Co(NO_3)_2$ show a single peak in a region between ~531.5−530.0 eV, indicating the O is in a hydroxide-like environment and thus a $Co(OH)_2$ local structure (Figure 1c; see Figure S7 for full range of films studied).[69,74,75] Upon addition of Fe, the O 1s spectra develop a shoulder at lower binding energy indicating O in a more-oxide-like environment (see arrow(s) in Figures 1c and S7), consistent with the presence of Fe^{3+} and thus more oxide bridges in the mixed-metal (oxy)hydroxide. Fe^{3+} is expected after exposure to oxygen in air.

After evolving O_2 from the electrodes at an *iR*-corrected overpotential of 350 mV for 2 h in 1 M KOH, the samples were re-examined by SEM and XPS (Figures 1b,c bottom row). For x = 0 the nanoplatelet structures appear less defined after conditioning. For x = 0.54 the structures remain largely unaffected. For x = 1 the structures appear to have largely dissolved as the bare Au substrate appears visible (see also Figure S8 for full range of compositions studied). The $Co_{1-x}Fe_x(OOH)$ films with x > ~0.5 also lost a portion of the film mass and showed decreased Fe:Co ratios (see Section 3.7). The O 1s XPS spectra of the anodically polarized films showed an increase in the size of the oxide-like shoulder at lower binding energies. This is consistent with an increase in the oxide character of the films due to the formation of CoOOH, FeOOH, and/or other Fe/Co-oxide phases. *In situ* measurements would be needed to determine the oxidation state under OER conditions. We discuss these structural and compositional changes in more detail when we address the electrocatalyst stability in Section 3.7.

3.2. Voltammetric Analysis of $Co_{1-x}Fe_x(OOH)$. The first CV cycle of all $Co_{1-x}Fe_x(OH)_2$ films for x < 1 has an anodic peak with a larger integrated area than either the corresponding cathodic peak or subsequent anodic peaks (Figures 2a and S9).

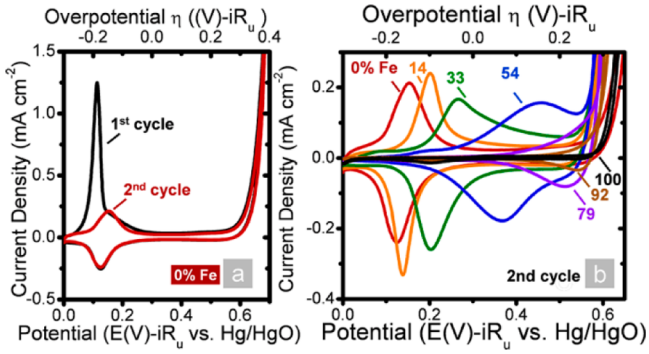

Figure 2. (a) Voltammetry of Co(OOH) in purified KOH showing the difference between the first and second CV cycle after deposition. (b) Voltammetry of $Co_{1-x}Fe_x(OOH)$ showing systematic anodic shift of the (nominally) $Co^{2+/3+}$ wave with increasing Fe content. The second CV cycle of each film is shown for clarity.

This peak has been seen in other $Co(OH)_2$ and CoO_x films and it has been attributed to an irreversible oxidation of $Co(OH)_2$ to CoOOH.[49,76] We also observe a decrease in film mass (~8%) only during this first anodic wave of the first CV cycle. It is likely that during the initial oxidation of the film, the mass decreases as NO_3^- ions exchange with OH^- (Figure S2).[73] This large anodic peak is not recovered during anodic cycling, anodic polarization, or after sitting in base with no applied potential for 120 min (Figure S10a). However, the peak does reappear upon cathodic cycling to −0.9 V vs Hg/HgO (Figure S10b). Such partial irreversible oxidation has been previously observed for $Ni(OH)_2$ oxidation to NiOOH and attributed to the trapping of the outer portion of the NiOOH film by electrically insulating $Ni(OH)_2$ formed at the underlying interface between the conductive electrode and film.[77] The conductivity switching behavior of $Co(OH)_2$/CoOOH is further discussed below.

DOI: 10.1021/jacs.5b00281
J. Am. Chem. Soc. 2015, 137, 3638−3648

As the Fe content in $Co_{1-x}Fe_x(OOH)$ films increases, the $Co^{2+/3+}$ wave shifts anodically (Figure 2b). This shift indicates a strong electronic interaction between the Co and Fe that modifies the electronic structure of the catalyst thus making Co^{2+} oxidation more difficult. This is consistent with the substitution of Fe onto Co sites in $Co(OH)_2$/CoOOH. We note that the Fe does not have any redox features in this potential range and remains nominally Fe^{3+}.[78] A similar effect on the Ni voltammetry is observed in Ni−Fe (oxy)-hydroxides,[53,55] and there have been related observations in various Co−Fe systems. Smith et al. noted a small redox wave in photochemically prepared $Fe_{0.4}Co_{0.60}O_x$ that was shifted ~0.4 V anodic relative to the wave assigned to CoO_x.[49] Laouini et al. added Fe to nanocrystalline Co_3O_4 films and observed a decrease in the integrated charge in the $Co^{2+/3+}$ wave with an increased lattice constant that was consistent with Fe incorporation into the nanocrystalline Co_3O_4.[44] An anodic shift in the $Co^{2+/3+}$ wave was observed with Ti incorporation into Co-based oxides; however, no increase in activity was reported.[79] The latter point is interesting, as it suggests that an anodic shift in the $Co^{2+/3+}$ wave alone is perhaps not sufficient to cause increased activity, an observation that will be discussed further in Section 3.6 with regard to the mechanistic role of Fe on the OER.

3.3. Intrinsic Activity via Turnover Frequency (TOF) Calculation. In order to make meaningful comparisons of activity trends and understand their fundamental origin, it is critical to compare intrinsic activities either on a TOF basis or normalized by real surface area.[6,16] The TOF is defined as the number of O_2 molecules produced per second per active site. A substantial challenge in measuring TOF is the difficulty in accurately measuring the number of active sites. Normalizing the current to the "real" surface area is also challenging as the real surface area is extremely difficult to measure, as has been discussed in detail by Trasatti.[80] McCory et al. suggested a standard protocol for assessing electrochemically active surface area by measurement of the double-layer capacitance in a potential region with no faradaic response.[17] This method, while suitable for electrodes consisting of conductive crystalline oxides without hydrated surface phases, fails for electro-deposited (oxy)hydroxide films. The electrode capacitance is nearly independent of the catalyst loading because ions polarize through the hydrated, electrolyte-permeated films against the underlying metallic electrode.[11,39,81,82]

To avoid the challenge in directly measuring active-site density, we have calculated TOF using the catalyst mass and composition provided from *in situ* QCM and *ex situ* XPS measurements, respectively. Figure 3a shows TOF_{mass}, which is calculated based on the total number of Co + Fe atoms from the steady-state current (assuming unity faradaic efficiency) at an iR_u-corrected η = 350 mV (Table S1 contains the complete data set). As some of the films are changing (i.e., losing Fe and/or chemically restructuring) the TOFs represent "snapshots" of activity after 1 and 120 min of steady-state polarization. TOF_{mass} is a *lower limit* for the TOF, as both Fe and Co sites are unlikely to be equally active and some cations are not electrochemically accessible. It is, however, the most practically relevant metric.

The CoOOH films (measured in a rigorously Fe-free electrolyte) showed TOF_{mass} = 0.007 ± 0.001 s^{-1}. The FeOOH films had a slightly higher TOF_{mass} = 0.016 ± 0.003 s^{-1}. $Co_{1-x}Fe_x(OOH)$ with x between 0.4 and 0.6 had TOF_{mass} ~ 100-fold higher, peaking at 0.61 ± 0.10 s^{-1} for $Co_{0.54}Fe_{0.46}(OOH)$. These data unequivocally demonstrate the synergistic role of Fe and Co for OER catalysis. We note that $Ni_{0.9}Fe_{0.1}OOH$ had a TOF_{mass} at η = 350 mV of 2.8 ± 0.4 s^{-1},[16] larger by a factor of >4 than for $Co_{0.54}Fe_{0.46}(OOH)$. Given the observation that the TOF can range over many orders of magnitude, these numbers are comparatively similar.

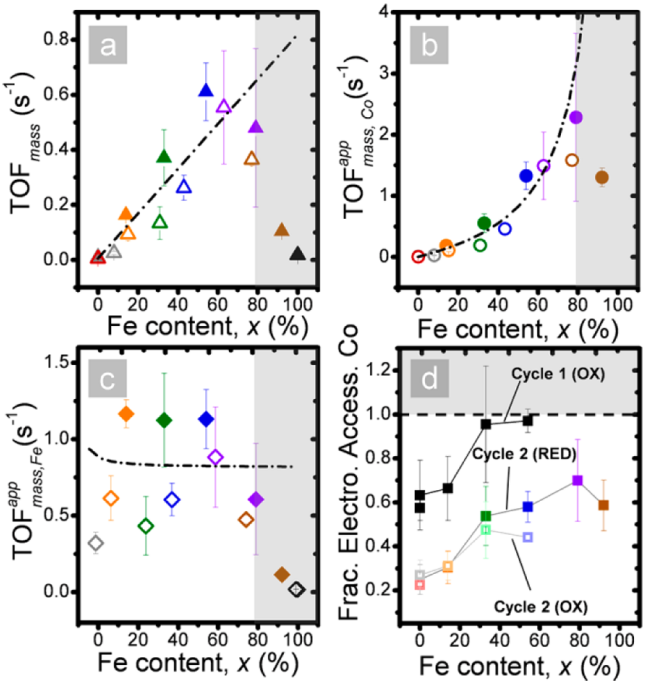

Figure 3. TOF data depicted based on the total film mass and composition assuming (a) all metal sites are available for catalysis (TOF_{mass}, triangles), (b) only Co-sites are available for catalysis ($TOF^{app}_{mass,Co}$, circles), and (c) only Fe-sites are available for catalysis ($TOF^{app}_{mass,Fe}$, diamonds) during steady-state polarization at η = 350 mV after 1 min (closed symbols) and 120 min (open symbols). Dot-dash lines (a−c) are calculations based on the model described in the text. Shaded regions indicate the region where the model no longer applies (see Section 3.6.2). (d) The fraction of electrochemically accessible Co is calculated from the ratio of the integrated charge of the cathodic $Co^{2+/3+}$ wave relative to the total Co deposited from mass measurements. Different symbols indicate integration of the oxidative peak (closed black squares) from the first CV cycle and the oxidative (open colored squares) and reductive peak from the second CV cycle (closed colored squares). Some data for x > 0.54 is omitted due to a lack of a distinct oxidation wave. Uncertainties (a−d) are standard deviations of three identically prepared samples (see Figure S1 for TOF determination and calculation). Some error bars are smaller than the symbols.

To better identify the metal centers responsible for catalysis, we separate TOF_{mass} into *apparent* TOFs for each element ($TOF^{app}_{mass,Co}$ and $TOF^{app}_{mass,Fe}$) by dividing by the relative Fe or Co atomic fraction, respectively (Figure 3b, c).

$$TOF^{app}_{mass,Fe} = \frac{TOF_{mass}}{x} \quad (1)$$

$$TOF^{app}_{mass,Co} = \frac{TOF_{mass}}{(1-x)} \quad (2)$$

These apparent TOF values thus implicitly assume that only one of the metal ions is active (e.g., Fe or Co).

To understand the activity trends of the various TOFs, we further analyzed the data under the simple assumption that

DOI: 10.1021/jacs.5b00281
J. Am. Chem. Soc. 2015, 137, 3638−3648

both Co and Fe (within the CoOOH host-structure) have a constant intrinsic activity (TOF^*_{Co} and TOF^*_{Fe}, respectively) for all x. To estimate TOF^*_{Co}, we take the average activity of pure CoOOH (~0.006 s^{-1}) as representative of the activity of Co-sites for all x. Due to the low electrical conductivity of FeOOH (see section 3.6.2), a reliable estimate of TOF^*_{Fe} cannot be taken from the pure FeOOH activity. From Figure 3c, we observe that $TOF^{app}_{mass,Fe}$ is nearly constant, within error, for $x \leq 0.79$, with an average value of 0.8 s^{-1} ± 0.3. We take this average $TOF^{app}_{mass,Fe}$ as TOF^*_{Fe}.

Using these intrinsic TOFs estimates, we then calculate the *expected* values for TOF_{mass}:

$$TOF_{mass} = (1 - x)\cdot TOF^*_{Co} + x\cdot TOF^*_{Fe} \quad (3)$$

as well as for $TOF^{app}_{mass,Fe}$ and $TOF^{app}_{mass,Co}$, using eqs 1 - 3. The *calculated* TOF data, assuming constant intrinsic activity TOF^*_{Co} and TOF^*_{Fe} with x, are overlaid as the dashed lines on the experimental data in Figure 3a–c. The agreement between the results of the simple model using experimentally derived TOF^*_{Co} and TOF^*_{Fe} as the only parameters for $x < 0.79$ suggests that the assumption of constant intrinsic activity for each cation is reasonable over this range. The substantial deviation from the model data for higher $x > 0.79$ (Figure 1a–c, gray regions) can be explained by the formation of phase-separated FeOOH (that is electrically insulating, as discussed below) within the active Co(Fe)OOH, similar to that recently described for Ni(Fe)-OOH.[57] More work would be needed to confirm this.

A separate method to estimate active site density is to integrate the total charge in a well-defined redox feature, for example associated with the $Co^{2+/3+}$ redox wave shown in Figure 2, and assume each electron is associated with a single surface-active metal ion. Counting active sites in this way, however, implicitly assumes the reaction occurs only on the metal exhibiting the redox feature (e.g., here Co), which we do not believe to be true. Furthermore, as discussed above, the size of the integrated redox wave is influenced by the scan cycle. Figure 3d shows the apparent fraction of electrochemically accessible Co centers (relative to the total number of Co from the mass measurement) as a function of Fe content and measurement cycle. The integrated charge in the Co oxidation measured on the first cycle represents 50–100% of the total Co in the film. On subsequent cycles, less of the film is apparently electrochemically active (~20–60%). As discussed above, this is likely due to trapping of a portion of the film in the oxidized state by an insulating Co–Fe hydroxide layer at the electrode surface. Because the oxidized film is conductive (see below) this portion of the film nevertheless remains OER active under operating conditions. These data confirm that a significant portion of the total number of Co sites is electrochemically accessible and thus indicate that the TOF_{mass}-based analysis presented above (which assumes all cations accessible) is reasonable.

3.4. Tafel Electrokinetics Analysis As a Function of Fe Content. Tafel analysis was performed on voltammetry data collected at 10 mV s^{-1}. This was used instead of steady-state measurements, because the $Co_{1-x}Fe_x(OOH)$ films change composition/activity with time. To minimize the contribution of noncatalytic current (i.e., faradaic and capacitive charging currents) we averaged the forward and reverse voltammetry sweeps prior to finding the Tafel slope (see Figure S12). The pure Co films have Tafel slopes of ~62 mV dec^{-1}. The films with moderately high Fe content ($0.33 < x < 0.79$) have Tafel slopes of 26–39 mV dec^{-1} (Figure 4). These slopes are similar to those observed in Ni(Fe)OOH thin films (25–40 mV dec^{-1}),[16,52,55] suggesting a similar mechanism for the OER in both systems.

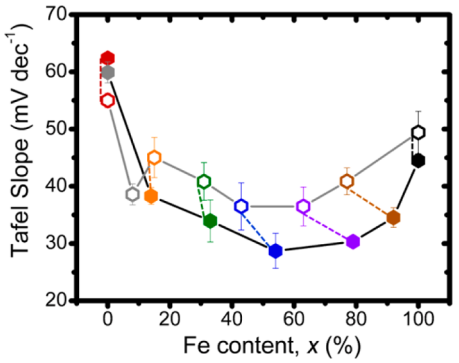

Figure 4. Tafel slopes from the second CV cycle (10 mV s^{-1}) taken before (solid circle) and after (open circle) a 2 h polarization at η = 350 mV (see Figure S12 for analysis details). Dotted lines are drawn to guide the eye to corresponding pre- and post-polarization values. Uncertainties are standard deviations of three identically prepared samples.

Traditionally, the Tafel slope has been used to infer which of the four electron-/proton-transfer steps are rate limiting in the OER.[25] The Tafel slope for a chemically reversible multistep reaction with a single rate-determining step (in the classical Butler–Volmer formalism) is given at room temperature by (59 mV dec^{-1})/($n' + \alpha$), where n' is the number of single-electron-transfer steps prior to the rate-determining step and α is the symmetry/transfer coefficient (typically taken as 0.5).[83] Thus, a Tafel slope near 40 mV dec^{-1} implies that the second electron transfer is rate determining, and a slope near 24 mV dec^{-1} implies the third electron transfer is rate determining. A Tafel slope near 60 mV dec^{-1} is associated with a rate-limiting chemical step following the first electron transfer.[32,84] While one can, in principle, thus infer changes in OER mechanism based on the observed changes in Tafel slope, we note that in Figure 4 there is a near-continuous change in the slope as a function of Fe content and electrochemical conditioning, suggesting the simple view of Butler–Volmer mechanistic kinetics may not be sufficient to describe the OER in this case.

3.5. Effect of Unintentional Fe-Incorporation from Electrolyte Impurities. The apparent OER activity of NiOOH is dramatically affected by small amounts of Fe impurities in basic electrolytes, causing a ~0.2 V cathodic shift in the OER onset potential.[52,53] For NiOOH, we found that precipitated $Ni(OH)_2$ was an effective absorbent to remove Fe from the electrolyte prior to testing.[53] There has been no previous work on the effect of electrolyte Fe impurities on OER catalysis on CoOOH. In the highest purity 1 M KOH available (TraceSelect/Semiconductor grade) we found that CoOOH films polarized at η = 350 mV for 2 h acquired 8% Fe by XPS (on a total metals basis, Figure S13) and that TOF_{mass} at η = 350 mV increased by roughly an order of magnitude (Figure 5). CoOOH catalysts polarized at η = 350 mV for 2 h in electrolyte purified using powder $Co(OH)_2$ as a Fe-absorbent (instead of $Ni(OH)_2$ as in our previous work)[53] showed no Fe incorporation by XPS and no activity increase. These results show that incorporation of Fe impurities increases OER activity on Co (oxy)hydroxide electrocatalysts. However, the activity increase (~10-fold) is less dramatic than for Ni (oxy)hydroxide

DOI: 10.1021/jacs.5b00281
J. Am. Chem. Soc. 2015, 137, 3638–3648

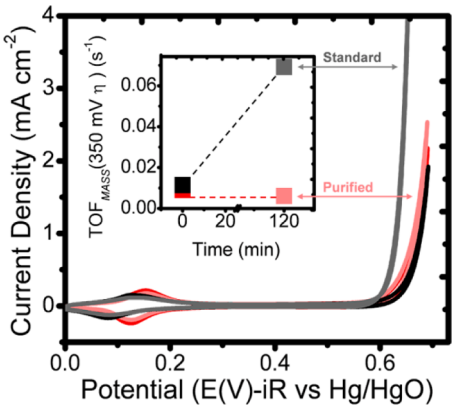

Figure 5. Voltammetry (second cycle) of $Co(OH)_2$ before (black and red, t = 0) and after 2 h of polarization at η = 350 mV in semiconductor grade (standard, gray) and purified (pink) 1 M KOH. TOF_{mass} at η = 350 mV is plotted in the inset. TOF_{mass} in this case is calculated based on the average of the current during the forward and reverse sweep at η = 350 mV.

(~100-fold) with similar Fe-impurity content and occurs more slowly (8% surface Fe incorporation in CoOOH after 2 h vs 5% surface Fe incorporation in NiOOH after ~10 min).[53]

Based on these results, it is likely that previous measurements of Co-based OER electrocatalysts in basic conditions were contaminated by low levels of Fe impurities. This could be important for mechanistic studies, because our data suggest the intrinsic activity of Fe is ~100-fold higher than that of Co in Co(Fe)OOH. For example, we previously reported the OER activity of a number of thin film OER catalysts, including CoO_x in 1 M KOH, whose surface likely partially converted to Co (oxy)hydroxide.[16] In that work we found a TOF_{mass} of 0.026 s^{-1} at η = 350 mV compared to 0.007 ± 0.001 s^{-} for rigorously Fe-free CoOOH studied here. This difference is consistent with low-level surface incorporation of Fe impurities below the detection limit of the XPS experiments used in the previous work. It is possible that similar Fe-impurity effects are also important in near-neutral buffered electrolytes, as has been observed for the NiOOH.[85] More work is needed to explore this possibility.

3.6. The Role of Fe in OER Catalysis in $Co_{1-x}Fe_xOOH$.

3.6.1. Structure and Electrolyte Accessibility. The data presented above show that Fe substantially increases the activity of Co (oxy)hydroxide. Furthermore, as x increases from 0 to 0.79 the fraction of electrochemically redox-active Co increases by nearly a factor of 3 (Figure 3d). Fe incorporation thus apparently allows for easier OH^- intercalation facilitating $Co(OH)_2 + OH^- \rightarrow CoOOH + H_2O + e^-$, which might be due to increased porosity/disorder. The diffraction data show that Fe incorporates into the layered (oxy)hydroxide structure and increases the spacing between the sheets, evident from the appearance of the low-angle reflection for the Co−Fe phase (Figure 1a). The increased electrochemical accessibility of Co alone, however, cannot explain the ~100-fold increase in TOF_{mass}. Fe might also increase the number of defect or edge sites on the Co oxyhydroxide structure, and it is possible that these are needed for OER.[34]

3.6.2. Effective Electrical Conductivity. Efficient electrocatalysis requires good electrical conductivity from the active site to an underlying metallic electrode.[13,53,86] Figure 6a shows the effective conductivity of $Co_{1-x}Fe_xOOH$ measured *in situ* using a dual-working-electrode configuration where the Co−Fe

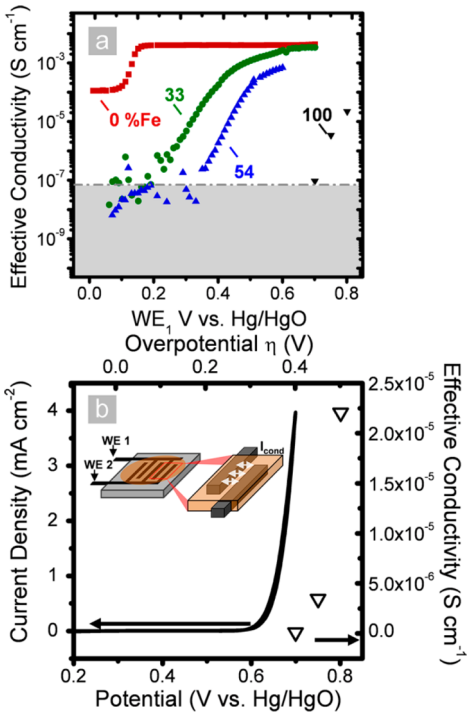

Figure 6. (a) Through-film conductivity as a function of Fe content. The gray-shaded area represents the region that has a smaller conductivity than the measurement limit in our approach. (b) Voltammetry of FeOOH (on a QCM electrode) overlaid with the conductivity of Fe measured on the interdigitated electrode. The OER current only becomes substantial once the conductivity becomes measurable. The inset schematic shows the interdigitated electrode with I_{cond} flowing between two working electrodes through the film.

(oxy)hydroxide film bridges two interdigitated microelectrodes.[53]

We use the term effective conductivity to account for the assumption that we have a dense, thick, and uniform slab of catalyst that allows for linear flow of electrons between the interdigitated arrays. This is likely the lower-bound of intrinsic catalyst conductivity. In the resting state (E < 0.1 V vs Hg/HgO) the films are insulators. The conductivity exhibits a sharp turn-on that is correlated in potential with the onset of the $Co^{2+/3+}$ oxidation wave. The addition of Fe shifts the oxidation wave and the turn-on in conductivity to more anodic potentials. Unlike Fe in NiOOH, Fe does not increase the electrical conductivity of $Co_{1-x}Fe_x(OOH)$ relative to CoOOH. The observed conductivity of ~4 mS cm^{-1} at OER potentials would lead to a potential drop of only ~0.25 mV across a 100 nm-thick film driving ~100 mA cm^{-2} of current. These data show that for $Co_{1-x}Fe_x(OOH)$ with x < 1 and for the thicknesses investigated here (~50 nm by cross-sectional SEM imaging), conductivity does not influence the measured activity.

The FeOOH films show dramatically lower conductivity than those containing Co. At potentials more cathodic than 0.7 V vs Hg/HgO (i.e., η < 400 mV), the conductivity is <10^{-7} S cm^{-1}, which is the measurement limit imposed by electrical noise. At higher potentials the conductivity increases, perhaps associated with the presence of mixed $Fe^{3+/4+}$ valencies and redox-hopping-type conduction.[87,88] This low conductivity has a dramatic effect on the measured catalysis. In order to drop <1 mV of potential across a film with a conductivity of 10^{-7} S cm^{-1} when passing 1 mA cm^{-2}, the film must be <l nm thick. It is therefore unsurprising that the onset of OER catalysis for

DOI: 10.1021/jacs.5b00281
J. Am. Chem. Soc. 2015, 137, 3638−3648

FeOOH near 0.65 V vs Hg/HgO corresponds well with the potential where the conductivity exceeds 10^{-7} S cm^{-1} (0.7 V vs Hg/HgO). At more cathodic potentials, catalysis would be limited to the small number of electrochemically accessible Fe that are also in direct contact with the conductive electrode. This indicates that FeOOH is likely more intrinsically active than we report based on TOF_{mass}, which merits further study beyond the scope of this manuscript.

3.6.3. Is Fe the "Active" Site? The result that FeOOH has an intrinsic activity (TOF_{mass} = 0.016 ± 0.003 s^{-1} at η = 350 mV) that is higher than CoOOH (TOF_{mass} = 0.007 ± 0.001 s^{-1} at η = 350 mV) and NiOOH (TOF_{mass} ~ 0.01 s^{-1} at η = 400 mV)[53] *before* correcting for the low-conductivity limitations of FeOOH described above is consistent with our analysis of the TOF data in Figure 3 that suggested the intrinsic activity of the Fe cation sites TOF^{*}_{Fe} was ~130-fold higher than that of the of the Co sites, TOF^{*}_{Co}. We therefore hypothesize that Fe provides the primary OER active sites in the mixed phases, while CoOOH (and relatedly NiOOH) provides an inherently high-surface-area (due to the electrolyte-permeable layered-(oxy)hydroxide structure) and sufficiently electrically conductive (at OER potentials) scaffold within which the Fe can be atomically dispersed.

The observations here and in our previous study of Ni−Fe (oxy)hydroxides are consistent with this hypothesis. TOF_{mass} values for the Ni−Fe and Co−Fe (oxy)hydroxides are within a factor of 4, and the Tafel slopes are both near 30 mV dec^{-1}, suggesting similar intrinsic active-site activity and mechanism in both materials. We also note, however, that in both Ni−Fe and Co−Fe (oxy)hydroxides there is strong electronic coupling between Fe and Ni/Co as evidenced by the shifts in the Co and Ni redox potentials with Fe incorporation. It is difficult to test for corresponding changes to the Fe redox potentials induced by alloying with Ni/Co, as Fe does not exhibit clear reversible redox waves in the experimentally accessible electrochemical window. However, the local electronic structure of Fe incorporated in NiOOH or CoOOH is undoubtedly different from that in FeOOH which may affect OER intermediate energetics and the OER activity on the Fe site. This hypothesis is supported by density functional theory (DFT) calculations for Co-doped hematite Fe_2O_3 (0001) surfaces in which Co doping decreases the reaction potential for OER as compared to pure hematite.[89] We are unaware, however, of DFT calculations that explain the observation that FeOOH is more active than CoOOH. In the case of Ni(Fe)OOH, very recent *in situ* X-ray absorption measurements coupled with computational methods provide further evidence that Fe is the active site with an electronic structure modified by the NiOOH host.[57]

3.7. Stability of the Measured Catalyst Activity: Film Dissolution vs Chemical Transformation. The intrinsic activity analyzed in Section 3.3 is associated with the initial composition and structure of the as-deposited $Co_{1-x}Fe_x(OOH)$. From a fundamental perspective, it is useful to understand how the structure and activity evolves after prolonged OER, as it may illuminate the OER mechanism on these materials. From a practical perspective, stability is important for applications in water-splitting systems. McCrory et al., for example, used a < 0.03 V change in overpotential during a 2 h polarization as criteria for stability of OER catalysts.[17] Frydendal et al. recently developed a protocol for testing catalysts using an electrochemical QCM and inductively coupled plasma mass spectrometry to demonstrate that without measuring changes to the active catalyst mass or structure, it is not possible to understand the changes to the measured OER current.[90]

We study the stability of the catalyst *in situ* by measuring the OER current at η = 350 mV and simultaneously the mass of the catalyst film using the QCM electrode (Figure 8). We also characterized the films before and after polarization using SEM and XPS (Figure 1b,c) and compared their voltammetry (Figure S9).

$Co_{1-x}Fe_x(OOH)$ films with x < 0.5 show a mass increase of 1−7% during the 2 h stability test (Figure 7). A similar mass

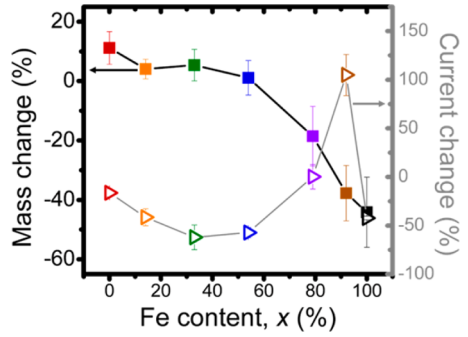

Figure 7. Percent mass (closed squares) and current change during 2 h polarization at η = 350 (error bars are standard deviations of three different samples).

increase (~0.3 μg cm^{-1}) was measured on a blank QCM electrode that was polarized for 2 h at η = 350 mV (Figure S3c). The OER current, however, was observed to decrease by 16 to 62% for these same samples (Figure 7). In many studies of OER catalysts, a similar decrease in current magnitude over time has been used to signify catalyst instability.[17] However, from the QCM mass measurements it is evident that the films are not dissolving. This change in activity over time could be due to a morphological/structural change that either reduces the number of active sites or limits access to them. For CoOOH, the integrated charge in the $Co^{2+/3+}$ wave (second cycle) decreases by ~8% during the 2 h of conditioning (Figure S9). This change might be due to the formation of local cobalt oxide domains with less electrolyte accessibility than the initial as-deposited $Co(OH)_2$/CoOOH. After polarization, the XPS data shows changes in the O 1s spectra also consistent with the formation of Co oxides. For the $Co_{1-x}Fe_x(OOH)$ with 0 < x < 0.5 the OER current drops in half over 2 h while the film mass and the integrated charge in the $Co^{2+/3+}$ wave is minimally affected. This would be consistent with minor structural rearrangements affecting the intrinsic site activity, although more work is needed to understand this effect.

$Co_{1-x}Fe_x(OOH)$ films with 1 > x > 0.5 slowly dissolve during the stability test, losing 18−38% of their mass during the 2 h. FeOOH (x = 1) is the least stable, losing ~44% of it mass. The OER current at η = 350 mV thus decreases over time for samples with x > 0.5. The TOF_{mass} for films with x > 0.43 (calculated with the mass measured *in situ*), however, increases over the 2 h stability test (Figure 8b). Further, the $Co^{2+/3+}$ wave potential is unchanged before and after conditioning, suggesting the composition of the electroactive Co−Fe (oxy)hydroxides is not changing. These data are consistent with the hypothesis that for $Co_{1-x}Fe_x(OOH)$ with x > 0.5 there are regions of FeOOH that have low activity (as they are electrically insulating). These regions then dissolve during stability testing

DOI: 10.1021/jacs.5b00281
J. Am. Chem. Soc. 2015, 137, 3638−3648

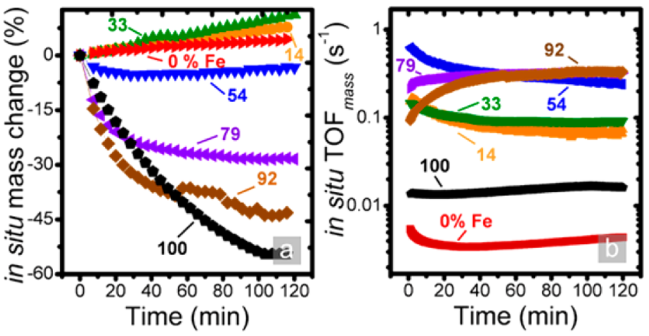

Figure 8. (a) *In situ* mass change as a function of time from films with the different Fe contents listed, and (b) semilog plot of activity normalized by the mass measured *in situ* with initial Fe content listed. The data are from the same representative sample for each film composition.

leading to a larger fraction of the film mass contributing to the OER. The data also demonstrate that CoOOH is responsible for chemically stabilizing Fe under OER conditions that would otherwise be soluble as FeOOH.

It is further interesting to consider the balance between stability and activity. Danilovic et al. compared the OER activity and stability of five different noble metal oxides in acid. They found that the most active metals were those with the least stability (i.e., high solubility in acid). The best catalysts, they argue, must balance stability and activity.[22] It is interesting to note that FeOOH is also unstable (i.e., soluble) unless incorporated into NiOOH or CoOOH, which are insoluble. This could indicate that the electronic/bonding effects that stabilize Fe within the Co matrix are the same as those that increase the activity of Fe-sites within mixed Co−Fe (oxy)-hydroxide systems above that of pure FeOOH.

4. CONCLUSION

We studied electrodeposited Co−Fe (oxy)hydroxides and discovered that Fe incorporation enhances the OER activity by ∼100-fold over that of pure CoOOH. We observed that Fe impurities incorporate into CoOOH unless test electrolytes are rigorously cleaned; of significance for the numerous mechanistic studies of Co-based OER catalysts. We combined *in situ* measurements of catalyst electrical conductivity and stability, along with *ex situ* diffraction and XPS measurements, to identify the roles of Fe and Co in $Co_{1-x}Fe_x(OOH)$ OER catalysis. FeOOH has a higher intrinsic OER activity than CoOOH but is an electrical insulator and is chemically unstable to dissolution under OER conditions in base. CoOOH is a good electrical conductor at OER potentials and chemically stable to dissolution. The voltammetry of $Co_{1-x}Fe_x(OOH)$ shows a strong dependence of the $Co^{2+/3+}$ potential on the Fe content, suggesting strong electronic coupling between Fe and Co in the solid. These data thus support a hypothesis where CoOOH provides a conductive, chemically stable, and intrinsically porous/electrolyte-permeable host for Fe, which substitutes for Co and serves as the (most) active site for OER catalysis. This work thus provides a new framework for understanding OER catalysis on transition metal (oxy)hydroxides and will aid in the design of improved OER catalysts.

■ ASSOCIATED CONTENT

Supporting Information

Table S1, Figures S1—S14, and calculations for associated figures are included in the Supporting Information. This material is available free of charge via the Internet at http://pubs.acs.org.

■ AUTHOR INFORMATION

Corresponding Author

*swb@uoregon.edu

Notes

The authors declare no competing financial interest.

■ ACKNOWLEDGMENTS

This work was supported by the National Science Foundation through CHE-1301461. M.G.K. and the thin-film X-ray diffraction analysis portion of this study were supported by the Center for Sustainable Materials Chemistry through the National Science Foundation grant CHE-1102637. The authors thank Lisa Enman and Adam Batchellor from the University of Oregon and Kathy Ayers, Julie Renner, and Nemanja Danilovic from Proton OnSite for insightful discussion. We acknowledge Stephen Golledge for help with XPS data interpretation. The project made use of CAMCOR facilities supported by grants from the W. M. Keck Foundation, the M. J. Murdock Charitable Trust, ONAMI, the Air Force Research Laboratory (FA8650-05-1-5041), the National Science Foundation (0923577 and 0421086), and the University of Oregon. S.W.B. thanks the Research Corporation for Science Advancement for support as a Cottrell Scholar.

■ REFERENCES

(1) Walter, M. G.; Warren, E. L.; McKone, J. R.; Boettcher, S. W.; Mi, Q.; Santori, E. a; Lewis, N. S. *Chem. Rev.* **2010**, *110*, 6446.
(2) Mckone, J. R.; Lewis, N. S.; Gray, H. B. *Chem. Mater.* **2013**, *26*, 407.
(3) Pletcher, D.; Li, X. *Int. J. Hydrogen Energy* **2011**, *36*, 15089.
(4) Armaroli, N.; Balzani, V. *Angew. Chem., Int. Ed. Engl.* **2007**, *46*, 52.
(5) Lewis, N. S.; Nocera, D. G. *Proc. Natl. Acad. Sci. U. S. A.* **2006**, *104*, 15729.
(6) Trotochaud, L.; Boettcher, S. W. *Scr. Mater.* **2014**, *74*, 25.
(7) Rossmeisl, J.; Qu, Z.-W.; Zhu, H.; Kroes, G.-J.; Nørskov, J. K. *J. Electroanal. Chem.* **2007**, *607*, 83.
(8) Koper, M. T. M. *J. Electroanal. Chem.* **2011**, *660*, 254.
(9) Zeng, K.; Zhang, D. *Prog. Energy Combust. Sci.* **2010**, *36*, 307.
(10) Appleby, a; Crepy, G.; Jacquelin, J. *Int. J. Hydrogen Energy* **1978**, *3*, 21.
(11) Lin, F.; Boettcher, S. W. *Nat. Mater.* **2014**, *13*, 81.
(12) Trotochaud, L.; Mills, T. J.; Boettcher, S. W. *J. Phys. Chem. Lett.* **2013**, *4*, 931.
(13) Trasatti, S. *Electrochim. Acta* **1984**, *29*, 1503.
(14) Merrill, M. D.; Dougherty, R. C. *J. Phys. Chem. C* **2008**, *112*, 3655.
(15) Singh, A.; Spiccia, L. *Coord. Chem. Rev.* **2013**, *257*, 2607.
(16) Trotochaud, L.; Ranney, J. K.; Williams, K. N.; Boettcher, S. W. *J. Am. Chem. Soc.* **2012**, *134*, 17253.
(17) McCrory, C. C. L.; Jung, S.; Peters, J. C.; Jaramillo, T. F. *J. Am. Chem. Soc.* **2013**, *135*, 16977.
(18) Hernández-Pagán, E. a.; Vargas-Barbosa, N. M.; Wang, T.; Zhao, Y.; Smotkin, E. S.; Mallouk, T. E. *Energy Environ. Sci.* **2012**, *5*, 7582.
(19) Okada, T.; Xie, G.; Gorseth, O.; Kjelstrup, S. *Electrochim. Acta* **1998**, *43*, 3741.

DOI: 10.1021/jacs.5b00281
J. Am. Chem. Soc. 2015, 137, 3638−3648

(20) Ayers, K. E.; Anderson, E. B.; Capuano, C. B.; Carter, B. D.; Dalton, L. T.; Hanlon, G.; Manco, J.; Niedzwiecki, M. *ECS Trans.* **2010**, *33*, 3.
(21) Ayers, K. E.; Capuano, C. B.; Anderson, E. B. *ECS Trans.* **2012**, *41*, 15.
(22) Danilovic, N.; Subbaraman, R.; Chang, K.; Chang, S. H.; Kang, Y. J.; Snyder, J.; Paulikas, A. P.; Strmcnik, D.; Kim, Y.; Myers, D.; Stamenkovic, V. R.; Markovic, N. M. *J. Phys. Chem. Lett.* **2014**, *5*, 2474.
(23) Galán-Mascarós, J. R. *ChemElectroChem* **2014**, *4*, 1637.
(24) Subbaraman, R.; Tripkovic, D.; Chang, K.-C.; Strmcnik, D.; Paulikas, A. P.; Hirunsit, P.; Chan, M.; Greeley, J.; Stamenkovic, V.; Markovic, N. M. *Nat. Mater.* **2012**, *11*, 550.
(25) Doyle, R. L.; Godwin, I. J.; Brandon, M. P.; Lyons, M. E. G. *Phys. Chem. Chem. Phys.* **2013**, *15*, 13737.
(26) Ardizzone, S.; Trasatti, S. *Adv. Colloid Interface Sci.* **1996**, *64*, 173.
(27) Gerken, J. B.; McAlpin, J. G.; Chen, J. Y. C.; Rigsby, M. L.; Casey, W. H.; Britt, R. D.; Stahl, S. S. *J. Am. Chem. Soc.* **2011**, *133*, 14431.
(28) Kanan, M. W.; Nocera, D. G. *Science* **2008**, *321*, 1072.
(29) Lutterman, D. a; Surendranath, Y.; Nocera, D. G. *J. Am. Chem. Soc.* **2009**, *131*, 3838.
(30) Farrow, C. L.; Bediako, D. K.; Surendranath, Y.; Nocera, D. G.; Billinge, S. J. L. *J. Am. Chem. Soc.* **2013**, *135*, 6403.
(31) Mattioli, G.; Giannozzi, P.; Amore Bonapasta, A.; Guidoni, L. *J. Am. Chem. Soc.* **2013**, *135*, 15353.
(32) Bediako, D. K.; Costentin, C.; Jones, E. C.; Nocera, D. G.; Savéant, J.-M. *J. Am. Chem. Soc.* **2013**, *135*, 10492.
(33) García-Mota, M.; Bajdich, M.; Viswanathan, V.; Vojvodic, A.; Bell, A. T.; Nørskov, J. K. *J. Phys. Chem. C* **2012**, *116*, 21077.
(34) Bajdich, M.; García-Mota, M.; Vojvodic, A.; Nørskov, J. K.; Bell, A. T. *J. Am. Chem. Soc.* **2013**, *135*, 13521.
(35) Friebel, D.; Bajdich, M.; Yeo, B. S.; Louie, M. W.; Miller, D. J.; Sanchez Casalongue, H.; Mbuga, F.; Weng, T.-C.; Nordlund, D.; Sokaras, D.; Alonso-Mori, R.; Bell, A. T.; Nilsson, A. *Phys. Chem. Chem. Phys.* **2013**, *15*, 17460.
(36) Li, X.; Siegbahn, P. E. M. *J. Am. Chem. Soc.* **2013**, *135*, 13804.
(37) Chen, J.; Selloni, A. *J. Phys. Chem. C* **2013**, *117*, 20002.
(38) Risch, M.; Khare, V.; Zaharieva, I.; Gerencser, L.; Chernev, P.; Dau, H. *J. Am. Chem. Soc.* **2009**, *131*, 6936.
(39) Klingan, K.; Ringleb, F.; Zaharieva, I.; Heidkamp, J.; Chernev, P.; Gonzalez-Flores, D.; Risch, M.; Fischer, A.; Dau, H. *ChemSusChem* **2014**, *7*, 1301.
(40) McAlpin, J. G.; Surendranath, Y.; Dinca, M.; Stich, T. A.; Stoian, S. A.; Casey, W. H.; Nocera, D. G.; Britt, R. D. *J. Am. Chem. Soc.* **2010**, *132*, 6882.
(41) Du, P.; Kokhan, O.; Chapman, K. W.; Chupas, P. J.; Tiede, D. M. *J. Am. Chem. Soc.* **2012**, *134*, 11096.
(42) Risch, M.; Ringleb, F.; Kohlhoff, M.; Bogdanoff, P.; Chernev, P.; Zaharieva, I.; Dau, H. *Energy Environ. Sci.* **2015**, *8*, 661.
(43) Iwakura, C.; Honji, A.; Tamura, H. *Electrochim. Acta* **1980**, *26*, 1319.
(44) Laouini, E.; Hamdani, M.; Pereira, M. I. S.; Douch, J.; Mendonça, M. H.; Berghoute, Y.; Singh, R. N. *Int. J. Hydrogen Energy* **2008**, *33*, 4936.
(45) Grewe, T.; Deng, X.; Tuysuz, H. *Chem. Mater.* **2014**, *26*, 3162.
(46) Xiao, C.; Lu, X.; Zhao, C. *Chem. Commun.* **2014**, *50*, 10122.
(47) Kishi, T.; Takahashi, S.; Nagai, T. *Surf. Coat. Technol.* **1986**, *27*, 351.
(48) Smith, R. D. L.; Prévot, M. S.; Fagan, R. D.; Zhang, Z.; Sedach, P. a; Siu, M. K. J.; Trudel, S.; Berlinguette, C. P. *Science* **2013**, *340*, 60.
(49) Smith, R. D. L.; Prévot, M. S.; Fagan, R. D.; Trudel, S.; Berlinguette, C. P. *J. Am. Chem. Soc.* **2013**, *135*, 11580.
(50) Suntivich, J.; May, K. J.; Gasteiger, H. a; Goodenough, J. B.; Shao-Horn, Y. *Science* **2011**, *334*, 1383.
(51) May, K. J.; Carlton, C.; Stoerzinter; Kelsey, A.; Risch, M.; Suntivich, J.; Lee, Y.; Grimaud, A.; Shao-horn, Y. *J. Phys. Chem. Lett.* **2012**, *3*, 3264.
(52) Corrigan, D. A. *J. Electrochem. Soc.* **1987**, *134*, 377.
(53) Trotochaud, L.; Young, S. L.; Ranney, J. K.; Boettcher, S. W. *J. Am. Chem. Soc.* **2014**, *136*, 6744.
(54) Trasatti, S.; Lodi, G. *Electrodes of Conductive Metallic Oxides*; Elsevier: Amsterdam, 1981; Vol. *B*, pp 521−626.
(55) Louie, M. W.; Bell, A. T. *J. Am. Chem. Soc.* **2013**, *135*, 12329.
(56) Corrigan, D. A.; Conell, R. S.; Fierro, C. A.; Scherson, D. A. *J. Phys. Chem.* **1987**, *91*, 5009.
(57) Friebel, D.; Louie, M. W.; Bajdich, M.; Sanwald, K. E.; Cai, Y.; Wise, A. M.; Cheng, M.-J.; Sokaras, D.; Weng, T.-C.; Alonso-Mori, R.; Davis, R. C.; Bargar, J. R.; Norskov, J. K.; Nilsson, A.; Bell, A. T. *J. Am. Chem. Soc.* **2015**, *137*, 1305.
(58) Brownson, J. R. S.; Lévy-Clément, C. *Phys. Status Solidi* **2008**, *245*, 1785.
(59) Hu, C.-C.; Chen, J.-C.; Chang, K.-H. *J. Power Sources* **2013**, *221*, 128.
(60) Liu, Z.; Ma, R.; Osada, M.; Takada, K.; Sasaki, T. *J. Am. Chem. Soc.* **2005**, *127*, 13869.
(61) Sauerbrey, G. Z. *Z. Phys. A Hadron. Nucl.* **1959**, *155*, 206.
(62) Moulder, J. F.; Stickle, W. F.; Sobol, P. E.; Bomben, K. D. *Handbook of X-ray Potoelectron Spectroscopy*; Chastain, J., Ed.; Perkin-Elmer Corporation: Waltham, MA, 1992; pp 254−257.
(63) Schweitzer, G. K.; Pesterfield, L. L. *The Aqueous Chemistry of the Elements*; Oxford University Press: Oxford, 2010.
(64) Risch, M.; Grimaud, A.; May, K. J.; Stoerzinger, K. a.; Chen, T. J.; Mansour, A. N.; Shao-Horn, Y. *J. Phys. Chem. C* **2013**, *117*, 8628.
(65) Grimaud, A.; Carlton, C. E.; Risch, M.; Hong, W. T.; May, K. J.; Shao-horn, Y. *J. Phys. Chem. C* **2013**, *117*, 25926.
(66) Zhang, J.; Wang, X.; Ma, J.; Liu, S.; Yi, X. *Electrochim. Acta* **2013**, *104*, 110.
(67) Therese, G. H. A.; Kamath, P. V. *Chem. Mater.* **2000**, *12*, 1195.
(68) Ma, R.; Liu, Z.; Takada, K.; Fukuda, K.; Ebina, Y.; Bando, Y.; Sasaki, T. *Inorg. Chem.* **2006**, *45*, 3964.
(69) Yang, J.; Liu, H.; Martens, W. N.; Frost, R. L. *J. Phys. Chem. C* **2010**, 111.
(70) Liang, J.; Ma, R.; Iyi, N.; Ebina, Y.; Takada, K.; Sasaki, T. *Chem. Mater.* **2010**, *22*, 371.
(71) El-Batlouni, H.; El-Rassy, H.; Al-Ghoul, M. *J. Phys. Chem. A* **2008**, *112*, 7755.
(72) Ma, R.; Sasaki, T. *Adv. Mater.* **2010**, *22*, 5082.
(73) Rahbani, J.; Ammar, M.; Al-Ghoul, M. *J. Phys. Chem. A* **2013**, *117*, 1685.
(74) Mclntyre, N. S.; Cook, M. G. *Anal. Chem.* **1975**, *47*, 2208.
(75) Biesinger, M. C.; Payne, B. P.; Grosvenor, A. P.; Lau, L. W. M.; Gerson, A. R.; Smart, R. S. C. *Appl. Surf. Sci.* **2011**, *257*, 2717.
(76) Koza, J. A.; Hull, C. M.; Liu, Y.; Switzer, J. A. *Chem. Mater.* **2013**, *25*, 1922.
(77) Corrigan, D. A.; Bendert, R. M. *J. Electrochem. Soc.* **1989**, *136*, 723.
(78) Lyons, M. E. G.; Brandon, M. P. *Phys. Chem. Chem. Phys.* **2009**, *11*, 2203.
(79) Seitz, L.; Pinaud, B.; Norclund, D.; Jaramillo, T. F. Materials for Photoelectrochemical and Photocatalytic Solar-Energy Harvesting and Storage. Proceedings from the Materials Research Society Spring Symposium, San Francisco, CA, April 21−25, 2014; Materials Research Society: Warrendale, PA, 2014.
(80) Trasatti, S.; Petrii, O. A. *J. Electroanal. Chem.* **1993**, *321*, 353.
(81) Burke, L. D.; Sullivan, E. J. M. O. *J. Electroanal. Chem.* **1981**, *117*, 155.
(82) Mills, T. J.; Lin, F.; Boettcher, S. W. *Phys. Rev. Lett.* **2014**, *112*, 148304.
(83) Bard, A. J.; Faulkner, L. R. *Electrochemical Methods: Fundamentals and Applications*; 2nd ed.; John Wiley and Sons, Inc.: New York, 2001; p 115.
(84) Surendranath, Y.; Kanan, M. W.; Nocera, D. G. *J. Am. Chem. Soc.* **2010**, *132*, 16501.
(85) Smith, A. M.; Trotochaud, L.; Burke, M. S.; Boettcher, S. *Chem. Commun.* **2014**, advance article. DOI: 10.1039/C4CC08670H.
(86) Viswanathan, V.; Pickrahn, K. L.; Luntz, A. C.; Bent, S. F.; Nørskov, J. K. *Nano Lett.* **2014**, *14*, 5853.

DOI: 10.1021/jacs.5b00281
J. Am. Chem. Soc. 2015, 137, 3638−3648

(87) Wuelfing, W. P.; Green, S. J.; Pietron, J. J.; Cliffel, D. E.; Murray, R. W.; Hill, C.; Carolina, N.; June, R. V.; Re, V.; Recei, M.; September, V. *J. Am. Chem. Soc.* **2000**, *122*, 11465.
(88) Katz, J. E.; Zhang, X.; Attenkofer, K.; Chapman, K. W.; Frandsen, C.; Zarzycki, P.; Rosso, K. M.; Falcone, R. W.; Waychunas, G. A.; Gilbert, B. *Science* **2012**, *337*, 1200.
(89) Liao, P.; Keith, J. A.; Carter, E. A. *J. Am. Chem. Soc.* **2012**, *134*, 13296.
(90) Frydendal, R.; Paoli, E. a.; Knudsen, B. P.; Wickman, B.; Malacrida, P.; Stephens, I. E. L.; Chorkendorff, I. *ChemElectroChem* **2014**, *1*, 2075.

DOI: 10.1021/jacs.5b00281
J. Am. Chem. Soc. 2015, 137, 3638−3648